Ground-to-Ground Optical Communications Demonstration

A. Biswas[1] and S. Lee[1]

A bidirectional horizontal-path optical link was demonstrated between Strawberry Peak (SP), Lake Arrowhead, California, and the JPL Table Mountain Facility (TMF), Wrightwood, California, during June and November of 1998. The 0.6-m telescope at TMF was used to broadcast a 4-beam 780-nm beacon to SP. The JPL-patented Optical Communications Demonstrator (OCD) at SP received the beacon, performed fine tracking to compensate for the atmosphere-induced beacon motion and retransmitted a 844-nm communications laser beam modulated at 40 to 500 Mb/s back to TMF. Characteristics of the horizontal-path atmospheric channel as well as performance of the optical communications link were evaluated. The normalized variance of the irradiance fluctuations or scintillation index σ_I^2 *at either end was determined. At TMF where a single 844-nm beam was received by a 0.6-m aperture, the measured* σ_I^2 *covered a wide range from 0.07 to 1.08. A single 780-nm beam* σ_I^2 *measured at SP using a 0.09-m aperture yielded values ranging from 0.66 to 1.03, while a combination of four beams reduced the scintillation index due to incoherent averaging to 0.22 to 0.40. This reduction reduced the dynamic range of the fluctuations from 17 to 21 dB to 13 to 14 dB as compared with the OCD tracking sensor dynamic range of 10 dB. Predictions of these values also were made based on existing theories and are compared. Generally speaking, the theoretical bounds were reasonable. Discussions on the probability density function (PDF) of the intensity fluctuations are presented and compared with the measurements made. The lognormal PDF was found to agree for the weak scintillation regime as expected. The present measurements support evidence presented by earlier measurements made using the same horizontal path, which suggests that the aperture averaging effect is better than theoretically predicted. The temporal power spectral densities (PSDs) of the irradiance fluctuations show nominal agreement with theoretically predicted behavior. The focal-spot sizes of the 844-nm and 780-nm beams received at either end are reported and compared with atmospheric "seeing" predicted by theory. The limit in which the theories agree with measurements is inconsistent with certain assumptions that are made; removing these assumptions renders significant differences between theory and measurement. The measured peak-to-peak beam wander at TMF was 4 m as compared with the theoretical prediction of 0.8 m. The received optical power at each end validates the uncertainty*

---

[1] Communications Systems and Research Section.

The research described in this publication was carried out by the Jet Propulsion Laboratory, California Institute of Technology, under a contract with the National Aeronautics and Space Administration.

predicted by link analysis. The temporal beacon spot motion on the OCD focal-plane array, a charge-coupled device (CCD), caused by atmosphere-induced phase tilt was used to determine the PSD. These PSDs were used together with the OCD tracking model to predict the uncompensated error and were found to be in agreement with measured values ranging from 4.8 to 9.3 μ*rad. The beacon motion PSDs also showed a partial correlation (0.67) with the intensity fluctuations sensed by the OCD focal-plane array. The best bit-error rates measured at TMF were* 1×10^{-5} *and were limited mainly by beacon fades, though beam wander of the OCD beam also may have played a role.*

I. Introduction

Optical communications is being developed by the TMOD Technology Program in order to provide cost-effective service to an expanding set of future NASA missions. Optical communications technology is capable of higher data rates with lower-mass and -power flight terminals as compared with current rf technology. Moreover, significant bandwidth expansion in an unregulated portion of the electromagnetic spectrum may be utilized. The horizontal path demonstrations described in this article are conducted as a precursor to space-to-ground laser communications demonstrations, the eventual goal being validation of optical communications technology for NASA's deep-space applications. Optical communications links from spacecraft in deep space to Earth-based ground receiving stations currently are planned because the alternative approach of using orbiting large aperture receivers poses formidable technology and cost challenges. Therefore, optical communications systems design requires a thorough understanding of atmospheric channel effects on propagating laser beams. Extensive theoretical work with limited experimental validation [1,2] of atmospheric effects on laser-beam propagation has been reported. We plan incremental demonstrations using optical communication systems in order to test the extent of agreement with theory, thereby gaining the ability to design higher-performance systems.

As compared with horizontal-path links exceeding a 10-km range, space-to-ground links for satellite laser communications involve beam propagation through a lower air mass. Consequently, the impact of atmospheric turbulence effects is less severe than that encountered on horizontal links. On the other hand, space-to ground links usually involve dynamic tracking and pointing strategies in order to maintain line of sight and compensate for space platform vibrations and jitter. Ground to geostationary (GEO) orbiting spacecraft are an exception wherein the line of sight also is static. Other differences also arise because both receiver and transmitter are "immersed" in the atmosphere for horizontal links. This is equivalent to having a phase screen in front of both receiving and transmitting apertures instead of only the ground-receiving aperture in space-to-ground links. Beam wander of the transmitted laser and focal-spot distortions of the received beacon, which would be absent for a space-borne optical transceiver, are present in horizontal optical links. These differences complicate a direct comparison between horizontal and space-to-ground links. With regard to atmospheric effects, horizontal links provide a worst case of space-to-Earth links, especially when the spacecraft is near the horizon.

Notwithstanding these important differences, we believe that horizontal-link demonstrations do provide a cost-effective early systems evaluation of optical communications, particularly of the design aspects related to mitigating atmospheric effects. With this in mind, a horizontal-path (46-km) bidirectional optical link demonstration [3,4] was conducted in June and November of 1998. The link was established between Strawberry Peak (SP), Lake Arrowhead, California, and the JPL Table Mountain Facility (TMF) in Wrightwood, California. A 0.6-m-aperture telescope at TMF was used to broadcast a multibeam continuous wave (CW) beacon (780 nm) to Strawberry Peak. The Optical Communications Demonstrator (OCD) [5,6], a JPL-patented laboratory prototype terminal located at SP, was manually aligned to acquire the beacon on its focal-plane array. The acquired beacon spot was subject to atmospheric turbulence-induced intensity and position fluctuations. The OCD transmitted a communications laser beam back to TMF while using the fine-steering control loop to compensate for atmosphere-induced beacon-spot motion.

The communications laser (840-nm) signal was modulated by a nonreturn-to-zero (NRZ) pseudorandom bit sequence (PRBS) at 40 to 500 Mb/s.

The demonstration objectives were to

(1) Evaluate received-signal irradiance fluctuations

(2) Measure and compare the focused spot sizes with those predicted by atmospheric seeing and angle-of-arrival fluctuation effects

(3) Validate link-analysis uncertainties at either end

(4) Evaluate the fine-tracking performance of the OCD

(5) Evaluate end-to-end link performance

A summary of theoretical predictions related to the measurements made in this demonstration along with a review of similar measurements made in previous demonstrations is given in Section II. The operational details along with a description of the setups used at either end of the link are described in Section III. Results, including comparisons with theoretical predictions, and discussions are in Section IV. Section V presents the conclusions and future plans.

II. Theory

Optical communications links must be designed to accommodate the myriad effects encountered during the passage of a laser beam through the Earth's turbulent atmosphere, without suffering outages. The dominant atmospheric effects are optical scintillation, angle-of-arrival fluctuations or phase tilt, beam wander, and beam spreading. Atmospheric attenuation of the laser beam due to absorption and scattering, which also results in loss of signal, is not discussed here. These effects will be addressed in a future article, utilizing data gathered from the Atmospheric Visibility Monitoring Stations [7].

A. Atmospheric Effects [1,2]

Random thermal fluctuations and wind in the atmosphere give rise to refractive index variations perturbing the propagation of a laser beam. The atmospheric channel is comprised of "atmospheric cells" or eddies of continuously varying size. The inner scale, l_0, and outer scale, L_0, set lower and upper bounds on these cell sizes. The L_0 value represents the size below which turbulent energy is injected into a region, while l_0 is associated with the smallest cell size before energy is dissipated into heat. Coherent laser beams propagating through the random phase media (atmosphere) undergo diffractive and refractive perturbations when interacting with the cells [8]. Qualitatively, cell sizes smaller than a beam diameter cause diffractive or interference effects, while those larger than a beam diameter cause refractive or focusing effects. Atmospheric turbulence models describe the power spectrum of refractive index fluctuations. Examples of these are the Kolmogorov and Von Karman spectra. A plane, spherical, or Gaussian optical wave front together with the choice of an atmospheric turbulence spectrum form the basis of the theoretical formulation of beam-propagation theory.

1. Optical Scintillation. Optical scintillation, a dominant observable effect, has a twofold effect: (1) temporal irradiance fluctuations sensed by a point detector receiving the laser beam after its passage through the atmosphere and (2) spatial intensity variations or speckle on a receiving aperture. Consider the temporal irradiance fluctuations first. Irradiance measurements of a laser beam, which traverses an atmospheric path, can be used to determine the normalized variance or scintillation index, σ_I^2, given by

$$\sigma_I^2 = \frac{\langle I^2 \rangle}{\langle I \rangle^2} - 1 \tag{1}$$

where I represents the measured irradiance and $\langle\,\rangle$ denotes an ensemble average. This can be related to a theoretically derived quantity known as the Rytov variance [Appendix, Eq. (A-1)], σ_R^2. The Rytov variance describes irradiance fluctuations experienced by an unbounded plane wave as it propagates through the atmosphere characterized by the Kolmogorov spectrum. As detailed in the Appendix, σ_R^2 can be used to characterize the strength of turbulence for an optical link. Thus, $\sigma_R^2 < 1$ corresponds to the weak fluctuation regime; $\sigma_R^2 \gg 1$ denotes strong turbulence; and, finally, $\sigma_R^2 \to \infty$ represents saturation. Exact analytical theories provide relations between σ_I^2 and σ_R^2 only in the weak fluctuation regime; however, asymptotic theories have been derived to extend the σ_I^2 dependence on σ_R^2 for diverse atmospheric conditions. These relations are summarized in the Appendix [Eqs. (A-2) through (A-4)]. Knowledge of σ_I^2 allows a determination of the dynamic range desired by the detector/sensor used to receive the laser signal in an optical link. Passage through the random phase media causes random fluctuations of the laser-beam amplitude; however, what is measured is the intensity. The intensities in the weak regime obey a lognormal distribution. Several mathematically complicated theories for the probability distribution function (PDF) universally applicable for weak-to-strong irradiance fluctuations have been reported [9,10]. With knowledge of the PDF, a determination of the fade statistics can be made, i.e., the probability of a fade exceeding a threshold dB level, the mean number of fades, and the mean duration of a fade [see Eq. (A-6)]. These quantities can be used to set bounds on the time-averaged bit-error and burst-error rates of an optical link. Finally, the temporal power spectral density (PSD) that can be determined by monitoring the irradiance provides knowledge of the frequency content of the irradiance fluctuations.

The second optical scintillation effect related to spatial intensity variations mentioned above is the atmospheric seeing described as λ/r_0, where λ is the optical wavelength and r_0 is called the Fried parameter or atmospheric coherence length. Equation (A-7) in the Appendix shows estimates of the spatial coherence length, ρ_0, from which r_0 is obtained by the simple relation $r_0 = 2.1 \times \rho_0$. The seeing limits the effective focal-spot size to $(2f\lambda/r_0)$ rather than the diffraction-limited $(2f\lambda/D)$, where D is the receiving-aperture diameter. Typical r_0's of a few centimeters render the focal-spot size to many times larger than the diffraction limit. The random intensity fluctuations observed at the focal plane cause "hot spots" to appear randomly in different spatial regions so that the effective centroid of the spot moves. A short-exposure blur circle can be described to enclose all the energy.

2. Angle-of-Arrival Fluctuations. Angle-of-arrival fluctuations (see Eq. (A-8) in the Appendix) due to random atmosphere-induced tilts of the optical wave front at the receiving aperture cause the spot to undergo random motion, also called "image dancing," in the focal plane. The combined spot motion and seeing effects define a long-exposure blur circle over which the optical energy is distributed. Optical detectors must be large enough to efficiently gather all the distributed optical energy in the blur circle. For very high data rate communications, this need conflicts with low detector capacitance (surface area) desired for high-bandwidth optical–electrical conversion. For optical transceivers like the OCD, which rely on beacon tracking, the image dancing and seeing cause beacon centroid motion on the focal plane. The fine pointing of the transmitted laser beam can be corrected so that reciprocity will ensure the arrival of the laser to the location from which the beacon originated.

The size of the collection aperture (see Eq. (A-9) in the Appendix) used to collect the laser signal after its passage through the atmosphere affects the observed intensity fluctuations. The larger the aperture size, the larger the number of speckles over which averaging occurs, with a net reduction of the intensity fluctuations sensed by a detector at the focal plane of the aperture.

3. Beam Wander. Beam wander (see Eq. (A-10) of the Appendix), on the other hand, occurs due to the presence of atmosphere near the transmitter aperture. Beam diameters smaller than atmospheric cell sizes are effectively deflected (refracted) by the varying refractive index eddies. Thus, when the beam has spread to scales larger than the atmospheric outer scale before encountering the atmosphere, such as in satellite-to-Earth communications, the beam wander effects are absent. On the other hand, beams originating from Earth telescopes, transmitted either to space or horizontally, usually have beam diameters smaller than the atmospheric cell sizes and are subject to beam wander. Beam wander may give rise to additional irradiance fluctuations for a Gaussian intensity-profile laser beam. This contribution is even more significant when the beam footprint is of the order of the receiving aperture size.

4. Beam Spreading. Beam spreading (see Eq. (A-11) in the Appendix) by the atmosphere spreads the energy density in the beam and contributes to additional dB loss in the link. The effective beam diameter can be thought of as a short-term beam diameter with random perturbations due to beam wander, so that the beam energy is spatially concentrated within a region of the effective beam diameter.

B. Previous Demonstrations

Although many horizontal-path optical-link experiments have appeared in the literature, we will discuss a few that are relevant to the current demonstration. A unidirectional optical-link demonstration was conducted jointly by Thermotrex and JPL [11], wherein an 80- to 250-μrad-divergence 810-nm laser beam was transmitted from SP to TMF in 1994. The received beam footprint at TMF was used to evaluate the effects of aperture averaging. Scintillation indices of 0.14 to 0.28 were measured for the largest aperture (28.7-cm diameter) used. The Thermotrex group [12] established a 150-km horizontal-path optical link between Mt. Haleakala and Mauna Kea at Hawaii. They reported scintillation indices in the range of 0.22 to 0.34. A group at the University of Central Florida [13] performed a reduced path length (183-m to 3-km) optical-link demonstration. They used the Cape Kennedy runway to measure scintillation indices well into the saturation regime of atmospheric turbulence and compared the measurements with theoretical models. A group at the Massachusetts Institute of Technology Lincoln Laboratories [14] demonstrated multibeam laser propagation using nine 488-nm beams over a 5.4-km range. A scintillation index reduction from 0.4–1.5 for a single beam to 0.1–0.18 using nine beams was reported.

Ground-to-satellite optical links also have been demonstrated. Some of these links used an uplink laser transmitted from the ground and reflected back to the ground from retroreflectors attached to low Earth-orbiting (LEO) spacecraft. The measured normalized variance σ_I^2 was representative of the uplink scintillation since the downlink contribution was negligible. The Low Power Atmospheric Compensation Experiment (LACE) [15] satellite was used for retroreflected links where σ_I^2 values ranging between 0.08 and 0.20 were measured. Furthermore, the temporal power spectral density showed a 30 times smaller contribution at frequencies >100 Hz as compared with 1 Hz. The Relay Mirror Experiment (RME) [16] also used retroreflectors on a near-Earth orbiting satellite to establish optical links. Scintillation indices, σ_I^2, ranging from 0.09 to 0.67 at frequencies ranging from 25 to 400 Hz were reported. The increase in higher-frequency contributions in the latter demonstration is noteworthy, although no space platform jitter results were provided in either of the two retroreflector space-to-ground links cited. Furthermore, in the RME, evidence was presented supporting the increase in σ_I^2 with off-axis pointing of the uplink beam (see Eq. (A-2) of the Appendix). A geostationary orbit laser communications demonstration (GOLD) was reported jointly by JPL and Communications Research Laboratory of Japan [17,18]. The laser communications terminal aboard the Japanese ETS-VI satellite was used. Scintillation indices of 0.18 or better were measured. GOLD used a four-beam 514.5-nm multibeam uplink, demonstrating for the first time the improvement in scintillation index that is achievable in ground-to-satellite links.

In the present demonstration, we are using a bidirectional link with laser beams being exchanged between a telescope and the optical communications terminal. This configuration has not been reported on previously. In addition to measuring the scintillation index at either end, we report on observed spot sizes (in order to evaluate seeing), link analysis, OCD fine-tracking, and, finally, a preliminary evaluation of end-to-end performance. Most of the horizontal-path demonstrations described above have been limited to scintillation-index measurements.

III. Demonstration Description

A. Operational Details

Figure 1 shows the 46-km-link range with a sectional view of the intervening terrain. The bidirectional optical path shown is almost entirely 2-km above sea level, providing relatively favorable atmospheric turbulence as compared with a sea-level horizontal link. A sturdy tripod located at SP was used for mounting the OCD assembly. The OCD assembly included a gimbal mount that facilitated manual control of OCD azimuth and elevation pointing; however, the gimbal was not electronically integrated and, therefore, could not be controlled by the OCD control-loop software.

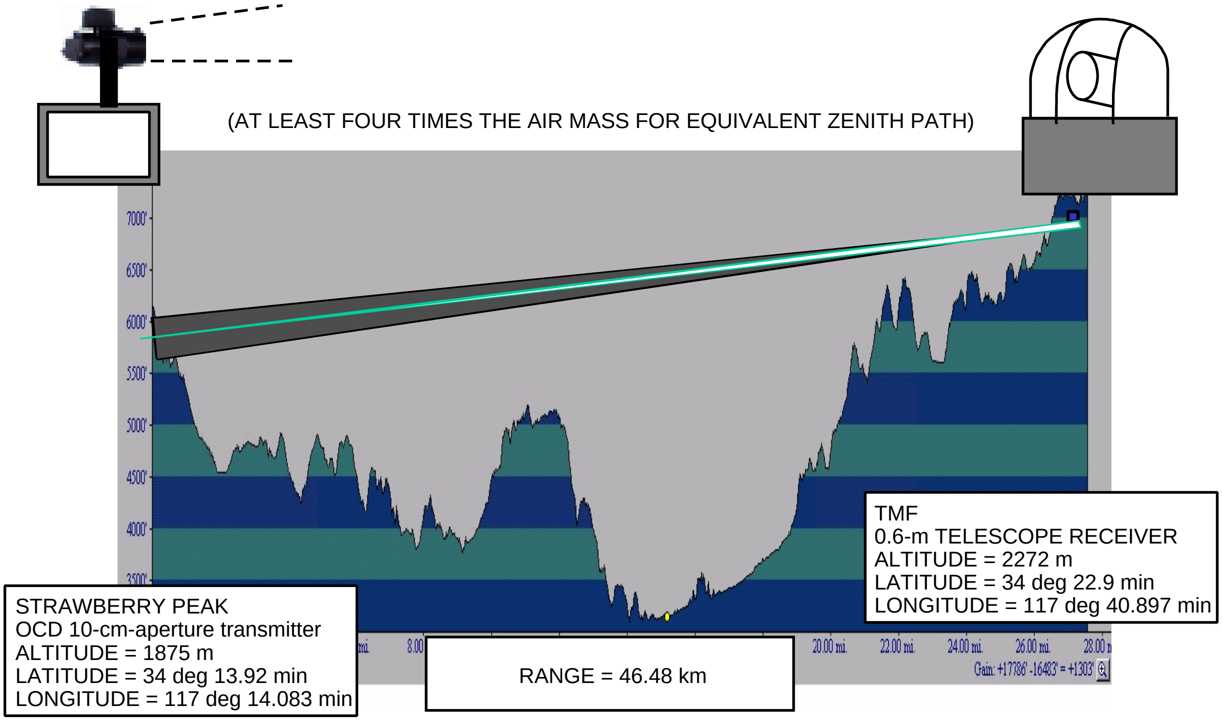

Fig. 1. A sectional view of the intervening terrain between TMF and SP.

The optical link was initiated by transmitting a multibeam beacon from the 0.6-m-aperture telescope at TMF to SP. Pointing relied upon knowledge of the 0.6-m TMF telescope settings required for locating SP. A co-bore-sighted 0.15-m spotting telescope with an intensified charge-coupled device (CCD) camera attachment capable of sensing a flashlight or electric lamp source at SP was used to validate the TMF telescope pointing. Use of the intensified camera, however, was restricted to nighttime backgrounds. Once the 0.6-m telescope was pointed to SP, a multibeam beacon (780 nm) comprised of four co-aligned beams was broadcast from TMF to SP. The details of the optical train used to accomplish this are described below.

Following beacon transmission, the OCD at SP was pointed to TMF by manual adjustments of the tripod and gimbal. The co-bore-sighted 0.15-m spotting telescope with an intensified camera at TMF was used to guide the OCD laser alignment. After the laser spot was sensed, manual adjustments of the elevation and azimuth of the OCD gimbal were made in order to increase the brightness of the laser spot on the intensified camera monitor. This was continued until the power meter located near the TMF coudé focus registered the OCD laser signal. The power received at TMF was maximized by further manual adjustment of the OCD gimbal azimuth and elevation. Finally, the OCD fine-steering mirrors were electronically stepped to achieve fine alignment with TMF. The latter step also resulted in acquisition and centering of the beacon spot in the OCD tracking sensor.

Once the static bidirectional link was established following the above procedure, several measurements could be performed. Irradiance fluctuations of the individual beacon beams as well as the combination of all four beams were recorded with spotting telescopes [see Fig. 2(a)].

The CCD camera that served as the OCD tracking sensor recorded images (single frames) of the received-beacon spot size. These were used to assess the atmospheric seeing effects on the spot size. The PSDs of the beacon spot motion, sensed by the CCD, also were measured using open-loop acquisition. These data sets, each containing 4000 centroid pairs (x- and y-axis at the focal plane) correspond to a duration of 2 s, since the 128-by-128 pixel CCD reads out subframes containing the regions of interest at 2 kHz. The centroids were computed using a 10-by-10 pixel window, where the angular extent of each pixel is 10 μrad. PSDs were computed using fast Fourier transform (FFT) operation as follows:

$$S(f) = \left| \, \mathrm{FFT}\big(x(t)\big) \right|^2 \Delta t^2 \tag{2}$$

where Δt is the sampling interval, 500 μs. Finally, the OCD control loop, using a two-axis fine-steering mirror (FSM) and the CCD, was activated. A fixed offset between the centroid positions of the received beacon and a bore-sighted transmit laser on the CCD was maintained by the control loop, while transmitting the high data rate on–off key modulated laser signal to TMF. Pseudo-random bit sequences (PRBS) represented by $2^N - 1$ (with $N = 7$ and 23) were used to modulate the OCD laser at 40 to 500 Mb/s. While in closed-loop operation, the OCD recorded beacon and transmit laser centroids at 1-s intervals.

At TMF, power and irradiance fluctuation measurements of the received communications laser signal were recorded. In addition, pupil images and focal-plane spots of the received 840-nm beam were recorded. Eye patterns and bit-error rate measurements also were performed on the communications laser signal.

B. SP Setup

Figure 2(a) shows a block diagram of the elements that comprised the SP setup. The OCD assembly mounted on a gimbal (not shown) had an optical interface with the laser transmitter and an electronic interface to the PC. An 844-nm optical-fiber-pigtailed diode capable of high-speed (500-Mb/s) on–off key modulation provides ~30 mW of average optical power to the OCD. Laser light emitted from the single-mode fiber is collimated and reflected off the FSM before being transmitted from the 10-cm-aperture telescope. A small bore-sighted fraction of the laser is focused on the CCD camera. Approximately 17 mW of optical power exits the telescope. The PC shown in Fig. 2(a) houses a digital signal-processing (DSP) board. The DSP board reads out (2-kHz) subframe CCD images from which relative centroid positions of the received beacon and bore-sighted transmit spots are determined. Control signals to the FSM amplifier are generated based on updated beacon positions. In Fig. 2(a), the spotting scopes (SS1 and SS2) are auxiliary Maksutov–Cassegrain telescopes with 90-mm clear apertures and a focal ratio of f/13.8. These telescopes were modified to accommodate 4-by-4-mm photodiodes that measured intensity fluctuations of the beacon beam transmitted from TMF. A storage oscilloscope was used to record the photodiode output while sampling at 1- to 2-kHz.

C. TMF Setup

Figures 2(b) and 2(c) show a schematic view of the optical train and a block diagram of the electronic interface, respectively, used in the TMF telescope coudé room. The coudé focus shown in Fig. 2(b) is established by pointing to a star at zenith (Vega was used). Ensuring that the receive-and-transmit light foci coincide with the coudé focus was used to verify transmit–receive co-alignment.

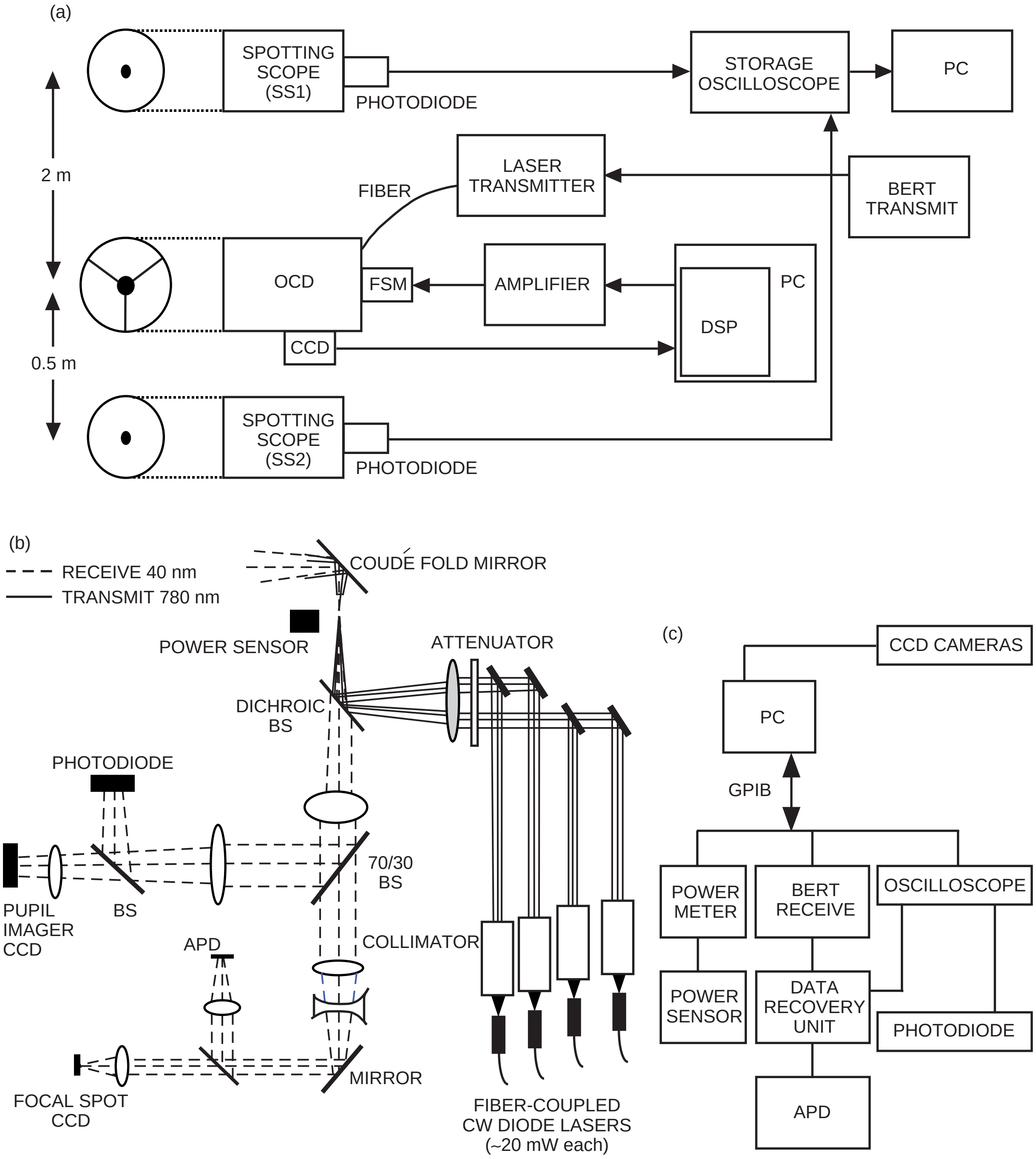

Fig. 2. Layouts: (a) the SP arrangement (spotting telescopes SS1 and SS2 are placed on either side of the OCD and used for acquiring beacon scintillation data); (b) the TMF coudé room optical panel; and (c) the coudé room electronic layout.

The multibeam beacon-transmit assembly used four thermoelectrically cooled (TEC) 780-nm diode lasers with a multimode fiber [62.5-μm diameter; 0.25 numerical aperture (NA)] coupled to the output. The power emitted at the fiber end was approximately 20 mW for each of these lasers. The output beams from each fiber were collimated and then guided with the aid of fold mirrors to a combining lens followed by a dichroic beam splitter (BS). The beams were brought to focus at the telescope coudé focus and then emerged from the TMF telescope primary mirror as four co-propagating 70- to 100-μrad divergence beams. The beam divergence was determined by estimating relative spot sizes at the coudé focus and the primary mirrors. Based on a 1-mm uncertainty in the relative positions of the beams at the coudé focus, the extent of co-alignment of the four beams was estimated to be 40 μrad.

As shown in the optical train of Fig. 2(b), the received signal at TMF was transmitted through the dichroic beam splitter and recollimated by a lens. The collimated beam was split by a 70/30 beam splitter. The reflected (30 percent) portion of the beam was used to record pupil images and perform irradiance fluctuation measurements. Pupil images were acquired at video frame rates with varying exposure times (30, 20, 10, 5, and 1 ms) using a CCD camera and frame grabber. Irradiance fluctuations were measured using a photodiode (4-by-4-mm square), sampled at 1 to 5 kHz by a digitizing oscilloscope. The collimated beam fraction transmitted by the 70/30 beam splitter was guided and focused on an avalanche photodiode (APD) integrated with a transimpedance amplifier. The APD active area was 500 μm, with a bandwidth of 450 MHz and a voltage conversion gain of 170 kV/W. The APD maximum noise equivalent power (NEP) is 0.6 nW (-61 dBm) at 450 MHz. The APD output is fed to a limiting amplifier requiring a minimum 15-mV peak-to-peak signal. The limiting amplifier output is fed to a clock and data-recovery circuit. A flip mirror was used near the APD to periodically record the focal spot received at TMF on a CCD camera. A power meter near the coudé focus was used for measuring power. A retroreflector was used to redirect the beacon laser spots into the receive assembly in order to check receive–transmit co-alignment.

The electronic interface block diagram [Fig. 2(c)] shows the data acquisition and recording arrangement. The CCD camera output was connected to a frame-grabber card in the PC. The APD output was fed to a clock and data-recovery (CDR) assembly. The resulting CDR outputs were used for viewing eye patterns on a 12-GHz bandwidth oscilloscope or, alternatively, for performing bit-error rate (BER) measurements. The bit-error rate tester (BERT), digital oscilloscopes, and power meter are interfaced over a general purpose interface bus (GPIB) and allow storage of data on the PC hard drive.

Figure 3 shows a collage of photographs relevant to the demonstration: Fig. 3(a) is the 0.6-m telescope dome at TMF; Fig. 3(b) shows TMF as seen from SP; Fig. 3(c) shows the coudé room optical assembly used to receive and perform diagnostics on the communications laser signal; and, finally, Fig. 3(d) shows the OCD mounted on the tripod at SP. One of the two spotting telescopes (SS1) also is shown in Fig. 3(d).

IV. Results and Discussions

A. Atmospheric Scintillation Predictions and Measurements

Equation (A-1) was used to calculate theoretical σ_R^2 values for the optical link. The atmospheric structure parameter, C_n^2, was estimated using the Air Force Geophysical Laboratories (AFGL) CLEAR I Night model [6]. For elevations of interest, from 1.8 to 2.3 km (see Fig. 1), the predicted C_n^2 range is from 1×10^{-16} to 5.2×10^{-17} m$^{-2/3}$. Using this range of C_n^2, theoretical bounds on σ_R^2 for the beacon and OCD laser beams were calculated as shown in Table 1. In the Appendix, Eqs. (A-2) through (A-4) present a number of possible relations between σ_I^2 and σ_R^2; all of these also were calculated in Table 1. Equation (A-2) extends the weak fluctuation theory to include the case of a Gaussian wave-front beam. This relation also predicts a spatial dependence of σ_I^2—in other words, an increase in scintillation index with mispointing. However, this relation is strictly valid for $\sigma_R^2 < 1$. Equations (A-3) and (A-4) are valid [8] for $0 < \sigma_R^2 < \infty$, with Eqs. (A-3a) and (A-3b) representing plane and spherical wave fronts when inner scale effects are neglected and Eqs. (A-4a) and (A-4b) representing plane and spherical wave fronts with nonzero inner scale effects. An atmospheric inner scale, $l_0 = 10$ mm, was used in Eq. (A-4). Figure 4 presents graphs of the predicted relation between σ_I^2 and σ_R^2 for parameters relevant to our optical link. When atmospheric cells of the order l_0 do not contribute to scintillation, both plane and spherical wave [Eqs. (A-3a) and (A-3b)] σ_I^2 reach maxima close to 1.2–1.4. Including inner-scale effects and assuming $l_0 = 10$ mm, on the other hand, predicts a continued increase in σ_I^2 as a function of σ_R^2 over the range shown. As l_0 decreases, the increase in σ_I^2 predicted by Eqs. (A-4a) and (A-4b) becomes less steep (not

Fig. 3. Demonstration photographs: (a) the 0.6-m telescope used as a receiver at TMF, (b) TMF viewed from SP (TMF is indicated by the arrow); (c) the optics assembled at the coudé room at TMF, and (d) the OCD mounting arrangement used at SP (SS1 is also shown).

Table 1. Predicted values of the Rytov variance, σ_R^2, and scintillation index, σ_I^2, from Eqs. (A-2) through (A-4) of the Appendix.

Beam	C_n^2 $\left(m^{-2/3}\right)$	σ_R^2	σ_I^2 (Gaussian approximation)	σ_I^2 (plane wave, no inner scale effects)	σ_I^2 (spherical wave, no inner scale effects)	σ_I^2 (plane wave, nonzero inner scale effects)	σ_I^2 (spherical wave, nonzero inner scale effects)
TMF to SP,	5.2×10^{-17}	2.677	1.085 to 1.091	1.081	0.888	1.111	0.95
780-nm	1×10^{-16}	5.078	2.059 to 3.069	1.203	1.294	1.293	1.470
SP to TMF,	5.2×10^{-17}	2.442	0.968 to 0.977	1.055	0.831	1.07	0.888
844-nm	1×10^{-16}	4.631	1.835 to 1.892	1.191	1.239	1.265	1.383

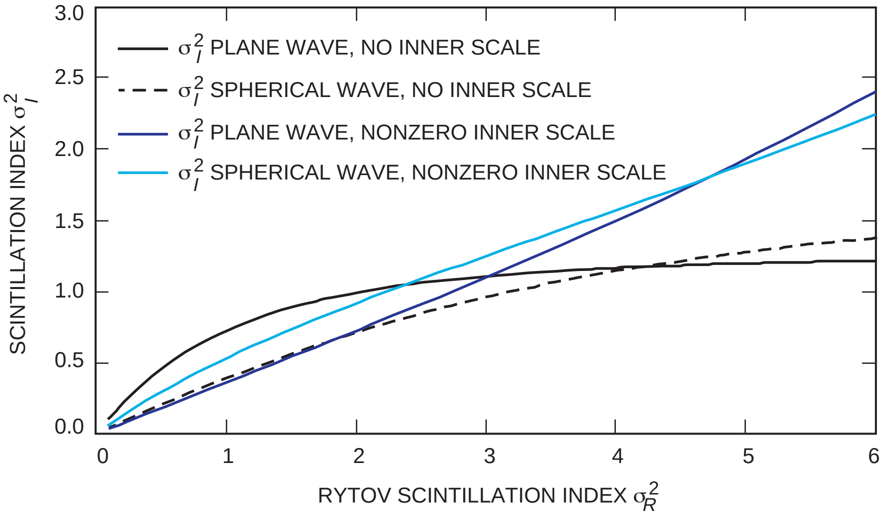

Fig. 4. The relation between the Rytov variance and the scintillation index according to the proposed theory [7], showing plane- and spherical-wave approximations with and without inner scale effects (see Eqs. (A-3) and (A-4) in the Appendix).

shown). From Table 1, one can see that the theoretical bounds on σ_I^2 are approximately from 0.97 to 1.9 for the SP-to-TMF beam (844 nm) and from 0.89 to 3.07 for the TMF-to-SP laser single beams (780 nm). However, if the σ_I^2 derived from the Gaussian approximation of weak fluctuation theory [Eq. (A-2)] is neglected, then these ranges change to from 0.83 to 1.38 and from 0.89 to 1.47.

Table 2 shows the normalized variance measurements made at TMF (SP-to-TMF beam) during June and November 1998. The November data were sampled at 5 kHz and gathered for 4-s intervals, while the June data were sampled at 1 kHz and acquired for 50 s. σ_I^2 is observed to range from 0.07 to 1.08. However, prior to comparing this with theory, the aperture-averaging factor discussed below must be accounted for. The data were fitted to a lognormal distribution using a polynomial method [17]. Representative irradiance distributions along with the fit are shown in Figs. 5(a) and 5(b). The lognormal distribution that fits the data approaches an exponential for large σ_I^2 and a Gaussian for small σ_I^2. However, Figs. 5(a) and 5(b) represent two extreme realizations of irradiance fluctuations. (Fig. 5(c) is discussed below.) An overall assessment of the extent of fit observed is performed by comparing higher-order moments $\langle I^n \rangle / \langle I \rangle^n$ (n being an integer) with those predicted by lognormal theory for many realizations. For the TMF measurements, this is shown in Fig. 6(a) for $n = 3, 4,$ and 5 (Fig. 6(b) is discussed below). The solid lines are derived from theory [1] by substituting

Table 2. A summary of normalized variances measured at TMF during June and November 1998.

Date	Time	Measured σ_I^2
11/13/98	01:39:02	0.34
11/13/98	01:40:33	0.62
11/13/98	01:43:27	0.81
11/13/98	01:45:45	1.08
11/13/98	01:54:33	0.93
11/13/98	04:57:34	0.84
11/13/98	05:02:56	0.40
6/20/98	02:26:28	0.12
6/20/98	03:31:58	0.12
6/20/98	04:07:44	0.11
6/19/98	12:20:34	0.87
6/19/98	04:57:33	0.51
6/18/98	01:23:10	0.07
6/18/98	05:07:56	0.07
6/18/98	05:15:26	0.98
6/18/98	05:18:04	1.08
6/17/98	02:58:28	0.51
6/17/98	03:07:36	0.41
6/15/98	05:30:18	0.20
6/15/98	05:33:18	0.23

$$\frac{\langle I^n \rangle}{\langle I \rangle^n} = \mu^{n(n-1)/2} \tag{3}$$

where $\mu = \langle I^2 \rangle / \langle I \rangle^2$. Figure 6(a) shows that beyond $\sigma_I^2 = 0.6$, the deviation from lognormal behavior is apparent for $n = 4$ and $n = 5$. This observation agrees well with similar horizontal-path data gathered over shorter ranges (from 183 m to 3 km) at sea level, where C_n^2 was in the range of 10^{-14} $\mathrm{m}^{-2/3}$ [13]. It is noteworthy that $\sigma_I^2 = 0.6$ also corresponds to $\sigma_R^2 = 1$ for the plane-wave relation given by Eq. (A-3a) (plane wave with no inner scale effects) and shown in Fig. 4. As expected, the deviation from lognormal statistics occurs as the weak fluctuation regime of scintillation is exceeded. A few exceptions to this general observation are also evident in the data, suggesting that sometimes $\sigma_I^2 > 1$ can also show good fits to lognormal statistics.

A wide range of σ_I^2 (0.07–1.08) was observed, as shown in Table 2. Whether this spread is entirely due to changes in the atmosphere or is modified by some artifact of the measurement technique is not certain. On both June 18 and November 13, large changes in σ_I^2 are apparent in measurements made a few minutes apart. These variations do not correlate with wind-speed changes that also were recorded at TMF. Further discussion on the variation of σ_I^2 observed at TMF is carried out below.

Equation (A-9) of the Appendix shows a number of relations for predicting the aperture-averaging factor, A. These are plotted in Fig. 7 (solid lines) along with measurements made during the current

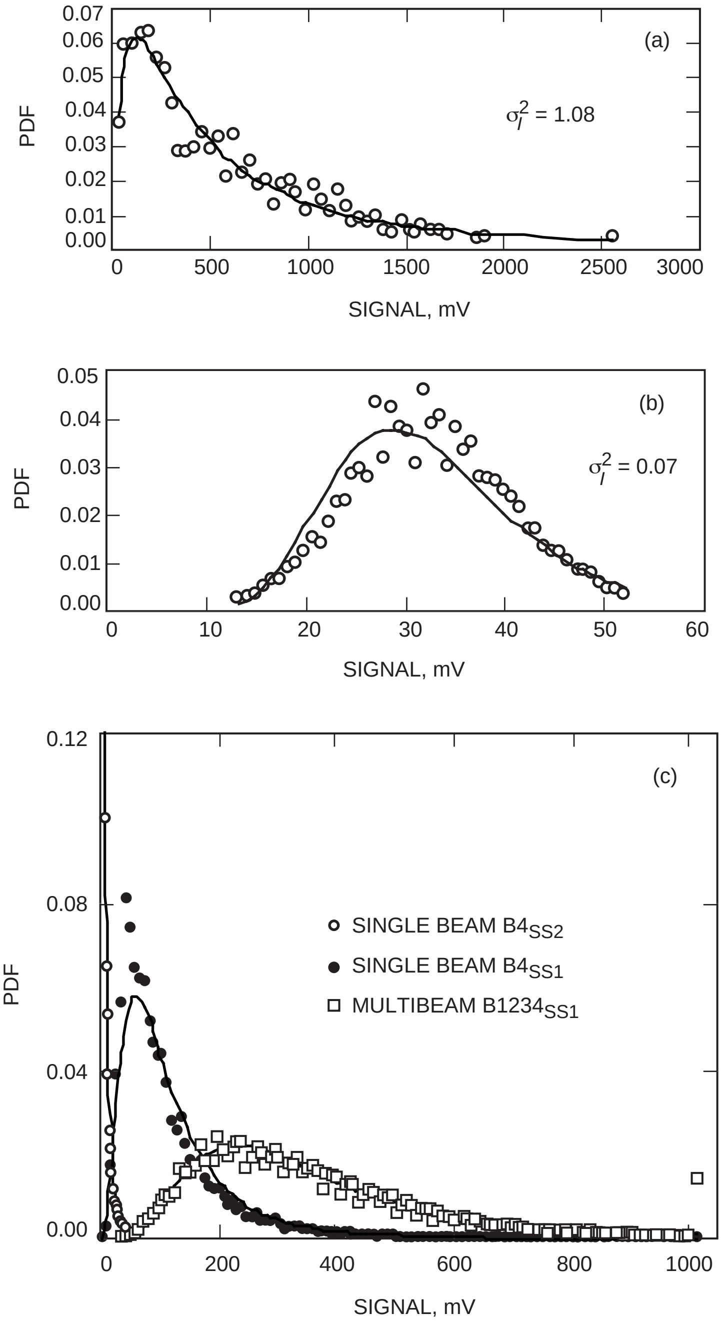

Fig. 5. PDFs: (a) with lognormal fit for irradiance fluctuations recorded at TMF for the 844-nm communications laser beam transmitted by OCD on November 13, 1998, at 1:45:45 with σ_I^2 = 1.08 and (b) on June 18, 1998, at 5:07:56 with σ_I^2 = 0.07, and (c) for irradiance fluctuation measurements made at SP for the 780-nm multibeam beacon broadcast from TMF.

demonstration (filled squares) and previous measurements (filled circles) also made at TMF in 1994. For the 1994 measurements, the signal-collection aperture in the pupil plane was varied in order to test aperture-averaging predictions. Current measurements were made with the full 0.6-m aperture. For the 1994 measurements, the scintillation index corresponding to $D = 0$ (D being the aperture diameter)

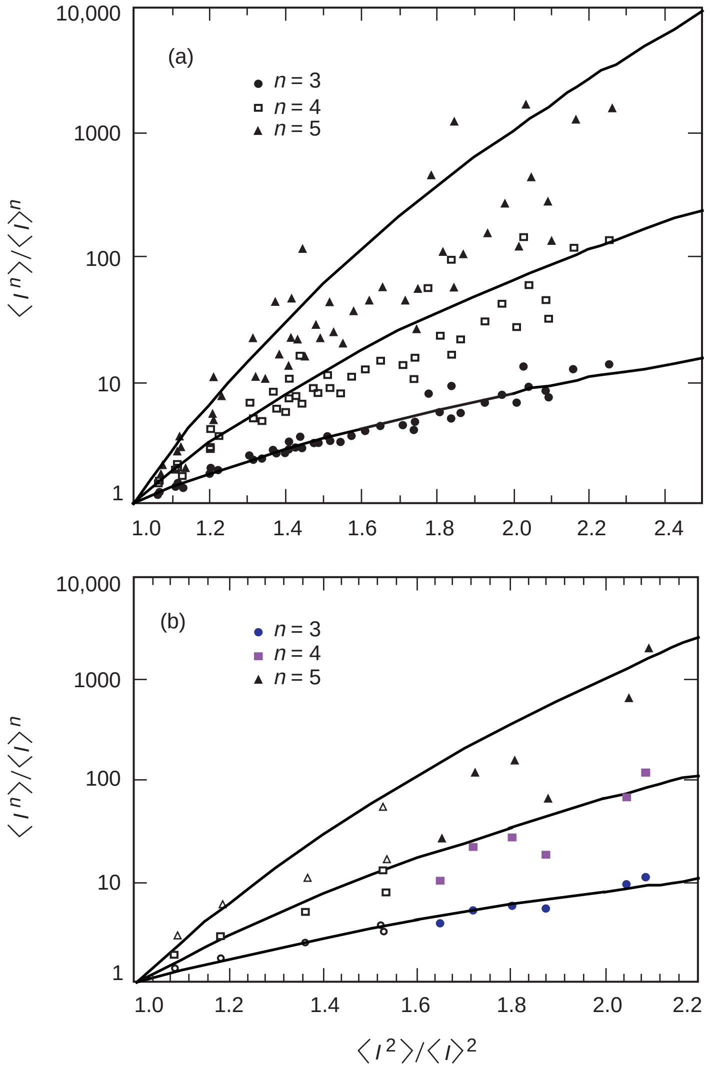

Fig. 6. Comparisons of (a) the measured higher moments (points) with lognormal theory predictions (solid lines) for the irradiance fluctuations recorded at TMF for the 844-nm OCD laser beam and (b) the irradiance fluctuations recorded at SP for single (filled points) and multibeam (clear points) beacons broadcast from TMF to SP.

was inferred by extrapolating σ_I^2 versus D. For the current measurements, the average theoretical σ_R^2 of Table 1 was used to infer the σ_I^2 corresponding to $D = 0$. The σ_I^2 measurements in 1998 span a large range but appear consistent with previous measurements and together suggest an aperture-averaging factor better than theory predicts.

After correction for the best theoretical aperture-averaging factor of 0.18 [Eq. (A-9b)], the theoretically determined σ_I^2 values of 0.97 to 1.38 in Table 1 will decrease to 0.16 to 0.56. However, an aperture-averaging factor of 0.08, as suggested by an imaginary line passing through the experimental points, will result in predicted σ_I^2 that range approximately from 0.08 to 0.11. The measured values range from 0.07 to 1.08. The lower range of measured values can be explained by invoking aperture averaging. Later in the text, beam wander is cited as a possible explanation for the higher range of σ_I^2 values measured.

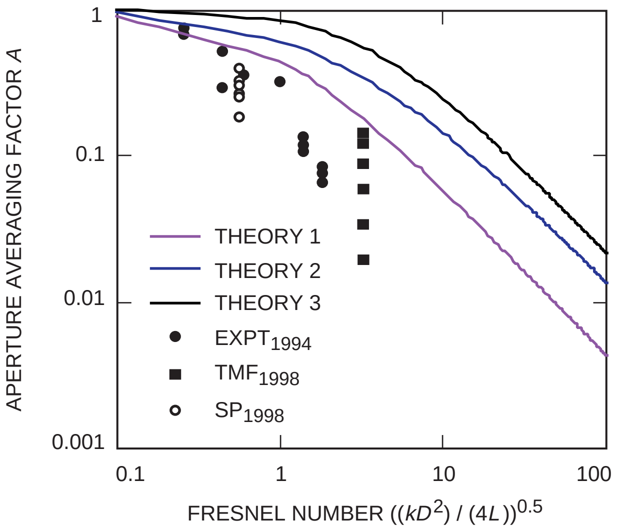

Fig. 7. A comparison of alternate theories of aperture averaging and measurements for optical links made between SP and TMF. The dark circles representing measurements made with varying aperture diameters were made in 1994, and the clear circles and dark squares were fixed-aperture measurements made in June and November 1998. The measurements provide strong evidence that theory underpredicts the reduction in the scintillation index.

Table 3 shows measurements made on four individual 780-nm beacon laser beams transmitted from TMF and received at SP. The normalized variances shown for the single beams (designated B1 through B4 and measured through spotting telescope SS1 or SS2) are all for June 18, 1998, between 10:00 and 11:00 P.M. These are fairly representative of a larger set of measurements made on different days in June (not shown). However, the measurements shown represent the most reliable beacon scintillation measurements. Measurements made on all four beams combined ($\mathrm{B1234_{SS1}}$ and $\mathrm{B1234_{SS2}}$) also are presented in Table 3. Representative irradiance distributions along with lognormal fits are shown in Fig. 5(c). At least one of the single-beam PDFs, although shown fitted to a lognormal distribution, probably would fit a negative exponential better. The PDF of the multibeam beacon also is approximated by a lognormal distribution, and the fit appears to be good. Figure 6(b) shows the higher moments plotted for the single (filled symbols) and multiple (clear symbols) beam scintillation-index measurements. The σ_I^2 values are higher (>0.6) for the single beam and lower (≤ 0.5) for the multiple beams.

The spatially separated measurements of the beacon intensity at SP suggested that all four beams were not perfectly overlapped at SP. It is noteworthy that the combination of the beacon beams, even though determined to be imperfectly overlapping in the far field, provided a significant reduction in σ_I^2. The predicted σ_I^2 for the combination of four beams determined by using Eq. (A-5) from the Appendix is 0.35 and 0.18 for the SS2 and SS1, respectively, as compared with the measured 0.34 and 0.22. The dynamic range of the irradiance fluctuations reduced from a range of 17 to 21 dB for single beams to a range of 13 to 14 dB for the combination. The larger deviation between measured and calculated values for SS1 is attributed to saturation of the photodetector at the peak irradiances observed in the individual beam measurements.

The beacon scintillation data with aperture averaging are shown in Fig. 7 (open circles). These data again reinforce evidence of the aperture-averaging factor being better than predicted by theory, falling along an imaginary curve intersecting the 1994 measurements and low σ_I^2 measurements made at TMF during the current demonstration.

Table 3. A summary of normalized variances measured at SP on June 18, 1998.

Date	Time	Beam	Measured σ_I^2
6/18/98	22:12:36	$B1_{SS1}$	1.03
6/18/98	22:12:52	$B1_{SS2}$	0.66
6/18/98	22:14:32	$B2_{SS1}$	0.76
6/18/98	22:14:44	$B2_{SS2}$	0.83
6/18/98	22:18:58	$B3_{SS1}$	0.753
6/18/98	22:19:16	$B3_{SS2}$	0.68
6/18/98	22:23:14	$B4_{SS1}$	0.72
6/18/98	22:24:04	$B4_{SS2}$	0.53
6/18/98	22:24:14	$B4_{SS1}$	0.72
6/18/98	22:41:36	$B1234_{SS2}$	0.35
6/18/98	22:41:18	$B1234_{SS1}$	0.22
6/18/98	04:38:46	$B1234_{SS2}$	0.40

The normalized temporal power spectrum of the irradiance fluctuations measured at SP and TMF are shown plotted in Fig. 8. Theory predicts a more or less flat power dependence on frequency until it exceeds the quantity $V(L \times \lambda)^{-1/2}$, following which it drops with a $f^{-8/3}$ dependence, V being the cross-wind velocity, L the range, and λ the wavelength. In the plots of Fig. 8, the power starts decreasing around 10 Hz, corresponding to a V of from 5 to 6 m/s. This value appears a little higher than the typical observed average wind speeds of from 1 to 3 m/s; however, wind gusts as high as 12 to 14 m/s also occurred. The slopes for the four plots shown are -2.5, -3.3, -2.3, and -1.5, as compared with the theoretical value of -2.66.

The beam wander of the laser transmitted by OCD was measured during open-loop operation after the link had been established. The beam footprint was projected on the telescope building wall by stepping the FSM on the OCD. Peak-to-peak beam wander was observed to be approximately 4 m, as compared with the predicted [Eq. (A-10)] maximum peak-to-peak value of 0.8 m. The beam-wander time period was of the order of 1 to 2 s. The beam shape projected on the TMF telescope wall was more elliptical than circular, with the minor axis being oriented vertically with respect to the ground. The measured beam-spot size (major axis times minor axis) was 1.67 × 0.9 m, as compared with the 1.2 m expected from beam-spreading theory [Eq. (A-11)].

The 844-nm beam footprint at TMF is only 1 to 2 times the primary mirror size. Pupil images viewed on the CCD camera in the coudé room show intermittent display of the pupil image, suggesting that the beam footprint overshoots the primary mirror periodically. When fine tracking of the OCD is turned on, the intermittence reduces significantly but does not go away. The intermittence of the pupil image observed at video rates occurred due to beam wander as well as to fades. Beam wander would contribute to additional irradiance fluctuations that could degrade the scintillation index. A distinguishing factor between beam wander and scintillation-related fades is the time scale. So, if beam wander were contributing to irradiance fluctuations, a larger low-frequency component would appear in the temporal spectrum. For comparison, the 780-nm beam footprint at SP is 3 to 4 m with respect to a collection aperture of 0.09 to 0.1 m. The beam footprint being many times the aperture size significantly reduces the contribution of beam-wander-related fades at SP. Therefore, comparing the temporal spectra at TMF and SP should show a larger low-frequency component at TMF as compared with SP. This is true of the spectra shown in Fig. 8, where the normalized peaks below 10 Hz are from 0.8 to 1 for

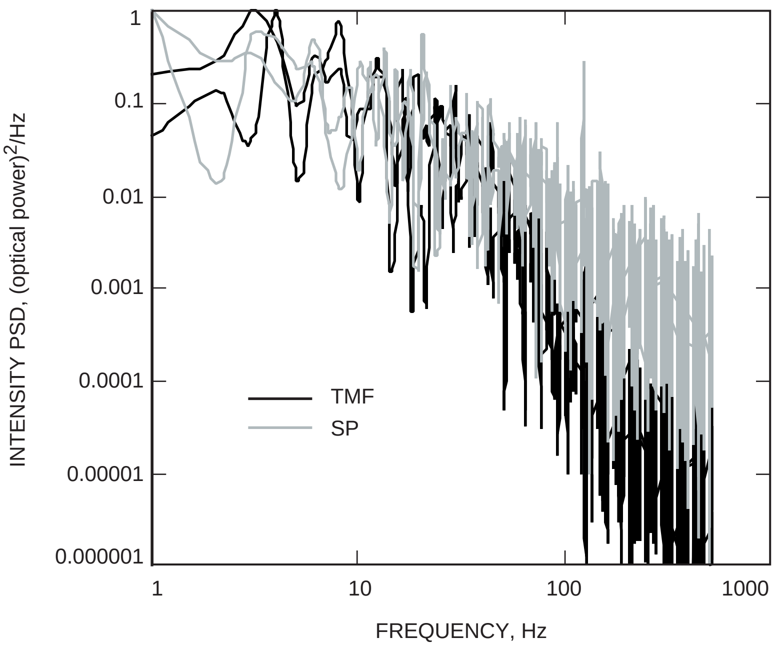

Fig. 8. Representative plots of the temporal PSDs determined using the intensity-fluctuation data recorded at TMF and SP.

TMF, as compared with from 0.4 to 0.6 for SP. This observation supports the conjecture that beam wander contributed to the observed larger values of σ_I^2 recorded at TMF but does not provide conclusive evidence. The very low σ_I^2 observations (0.07) at TMF would further suggest that the beam wander did not affect the irradiance fluctuations all of the time. Atmospheric variations could at times make the beam wander more dominant—for example, when there are wind gusts anywhere along the path—consequently giving rise to much larger σ_I^2.

Atmospheric coherence length, r_0, predictions for the OCD beam received at TMF can be made assuming a Gaussian or plane wave for the limits where ρ_0 is much smaller or much larger than the atmospheric inner scale, l_0 [see Eq. (A-7)]. All these approximations yield r_0 values ranging from 3.0 to 10 cm (a 1-mm atmospheric inner scale was assumed) with corresponding atmospheric seeing from 1.7 to 5.6 arcsec. The corresponding largest predicted focused spot sizes are 190 μm. In addition to the seeing effects, the angle-of-arrival fluctuations cause motion of the focal spot. The predicted maximum displacement of the spot center should be contained inside a circle with a diameter of approximately 100 μm at the TMF focal spot CCD. Thus, according to theory, the blur circle resulting from the combination of seeing and phase tilt (angle-of-arrival) fluctuations should not exceed 300 μm.

Spot sizes were measured at the focal plane using a CCD camera. On June 18 and 19, 1998, exposure times of 33 ms were used, while on November 13, 1998, exposure times of 1 ms were used. The mean spot diameter with longer exposure times was approximately 212 μm, while the shorter exposure yielded mean spot sizes of approximately 150 μm. The centroid motion of the spots never exceeded a maximum of 62 μm. Thus, the blur circle described by spot motion and seeing appeared to be contained at the very worst within a circle of 300 μm. The seeing estimate based on the measured values ranges from 4.3 to 6.7 arcsec. For comparison, TMF nighttime seeing typically ranges from 2 to 3 arcsec at zenith [17]. Note that the worst-case predictions of ρ_0 that are obtained by assuming the Cn^2 value of 1×10^{-16} m$^{-2/3}$ and using a plane-wave approximation in the limit $\rho_0 \ll l_0$ appear to best fit the measurements made. However, this approximation yields a ρ_0 that is larger than the assumed l_0 of 1 mm. On the other hand, if l_0 is assumed to be larger, then the spot sizes are under-predicted. This illustrates deficiencies of the theory in predicting measurements.

For the focal recieved spot on the OCD, the seeing predicts a spot size of from 57 to 93 μm, whereas the spot observed on the CCD varied from 40 to 100 μrad. This compares with from 20 to 30 μrad measured in the laboratory. Thus, the phase front perturbation contributes in a two to three times larger focal spot size.

B. Link Analysis

Nominal, best-case, and worst-case predictions of the average power expected at either end of the optical link were obtained by analysis. A comparison between measurements and predictions provides an assessment of the link uncertainties.

Figure 9(a) shows the comparison between optical power received through the two spotting scopes and the predictions for a single 70-μrad divergence, 20-mW beam transmitted from TMF. The system loss consists of the transmit–receive antenna gains, relay optics losses of the transmitting and receiving

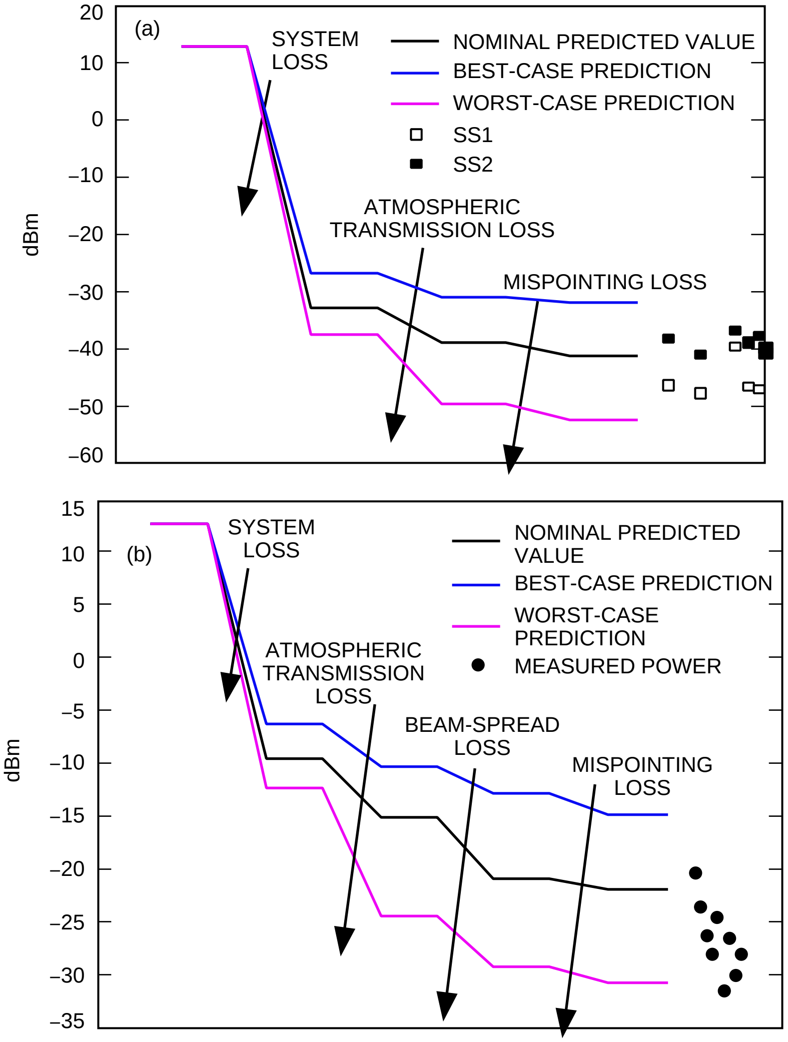

Fig. 9. Results of the link analysis as compared with measurements for (a) a single 100-μrad, 20-mW, 780-nm laser transmitted through a subaperture of the TMF telescope and received through the spotting scopes at SP and (b) the 22-μrad, 17-mW, 840-nm laser transmitted from OCD and received at the coudé focus of the TMF telescope.

telescope assemblies (the latter was verified in the laboratory while the former is based on specified reflectivity and expected performance degradation of the TMF telescope mirrors), and the space loss. The atmospheric losses are based on FOCAS [19] predictions for varying visibility conditions, while the pointing losses account for reasonable mispointing limits of the TMF telescope. The measurements agree well with nominal predictions. In general, power through SS2 [see Fig. 2(b)] measured approximately 5 dB more than SS1. This observation is consistent with the peak-intensity region of the beacon beam footprint being close to the OCD optical axis and SS1 being approximately 2 m away from this peak.

Figure 9(b) shows a comparison of the 840-nm optical power received at the coudé focus of the TMF telescope, with predictions. The system loss, atmospheric transmission loss, and pointing losses were obtained in a manner identical to that stated above. A beam-spread loss term is included since the effect of the atmosphere on the low-divergence, near-diffraction-limited beam exiting the OCD is non-negligible. Nighttime observations of the beam footprint received at TMF through an IR viewer supported these predictions. In general, the measured powers are lower than the nominal predictions. The largest source of uncertainty in this analysis is the TMF telescope throughput efficiency at 840 nm.

C. OCD Acquisition and Fine-Tracking Performance

The beacon-spot sizes observed on the OCD tracking sensor were described in Section IV.A. The motion of the spot on the CCD is best described by a determination of the PSDs. Ten data sets were acquired throughout the night of November 13, 1998. FFT operations described by Eq. (2) were performed. Table 4 shows the root-mean-square (rms) motion determined for each of the data sets. Two PSD plots, which represent the largest and smallest observed rms beacon motions, are shown in Fig. 10 (data sets 1 and 4 in Table 4). The PSDs of all the other data sets in Table 4 lie between these two cases. For comparison, the Olympus spacecraft vibration PSD [20] model (dotted lines) also is shown in Fig. 10. The mean rms value observed for the OCD beacon-spot motion (approximately 10 μrad for the x- and y-axes, or a root sum square (rss) of approximately 14 μrad radial) is slightly smaller than the Olympus spacecraft vibration, which has an rms value of 16 μrad radial. Beacon motion caused by atmospheric turbulence in our demonstration is referenced to spacecraft vibrations by this comparison, since the Olympus spacecraft vibration model often is used to validate fine-tracking performance for optical communication terminals.

Table 4. Beacon motion: uncompensated after OCD fine tracking and total rms motion.

Data set	RMS motion		Uncompensated motion	
	X-axis, μrad	Y-axis, μrad	X-axis, μrad	Y-axis, μrad
1	14.09	11.96	7.37	6.12
2	12.91	11.75	8.72	7.32
3	9.85	9.66	4.82	5.57
4	5.11	5.19	2.37	2.36
5	8.97	9.81	4.13	4.02
6	6.69	5.61	3.44	3.53
7	13.10	12.75	5.79	6.54
8	12.90	12.44	6.00	6.23
9	9.63	8.26	4.60	4.41
10	12.58	14.84	6.06	6.48
Mean	10.58	10.22	5.33	5.25

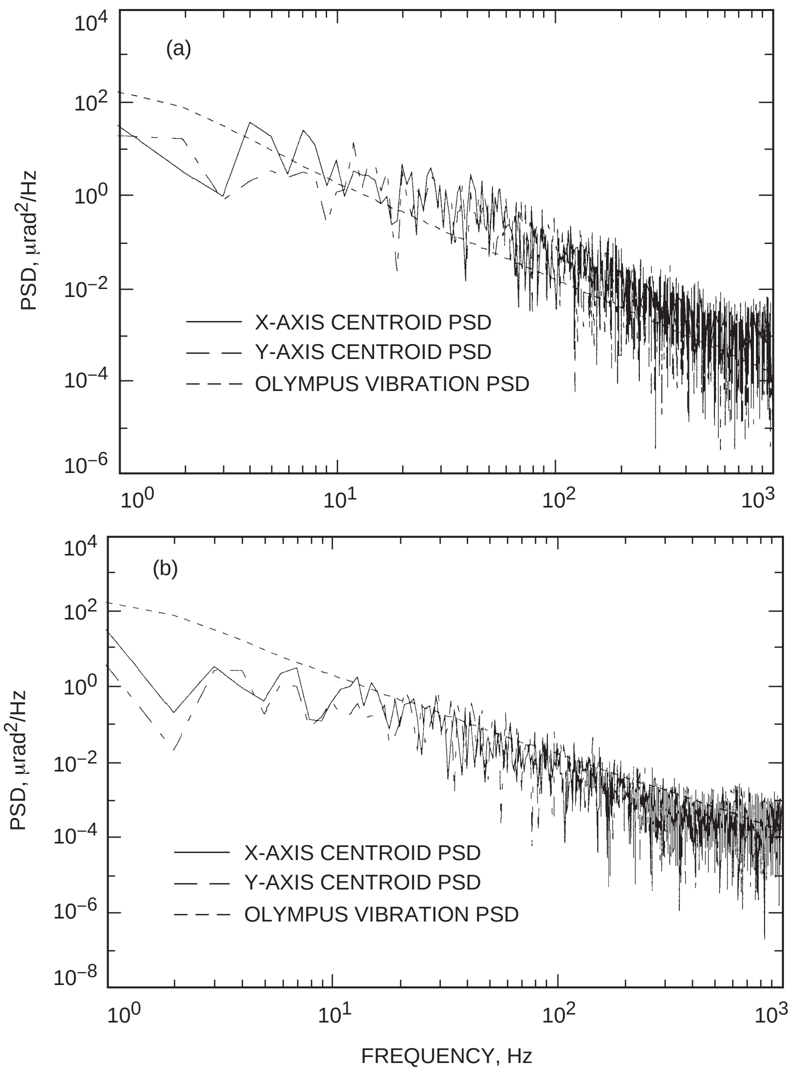

Fig. 10. The PSD representing the observed beacon spot motion on the OCD tracking sensor for the (a) largest and (b) smallest observed rms centroid displacement. The Olympus spacecraft PSD is included for reference.

Beacon motion was observed to decrease rapidly at higher frequencies. This was confirmed by the data in Table 5, where the cumulative sum at a few frequencies (μrad^2) is shown. For example, over 90 percent of beacon motion occurs at less than 50 Hz for x-axis beacon motion. The contribution beyond 100 Hz is negligible.

1. OCD Fine-Tracking Performance. The primary function of the OCD fine-tracking control loop is to track the beacon position using the CCD and feed this information back to the FSM such that it can update the transmit laser fine pointing to preserve a fixed offset between beacon and bore-sight centroids. This results in the transmit laser being pointed back to the direction from which the beacon arrived. The important performance parameter for the fine-tracking control loop is the disturbance rejection bandwidth that is defined as a 0-dB bandwidth for disturbance rejection. For the tracking to be effective, the disturbance rejection bandwidth should be sufficiently large to compensate the beacon motion. In the current demonstration, this motion is caused by the atmospheric turbulence; however, in a space-borne optical communications terminal, this will be caused by platform vibration and jitter.

Table 5. Ratio of energy (motion ^{2} × bandwidth) up to the given frequencies with respect to the total energy.

Data no.	10 Hz		50 Hz		100 Hz		200 Hz	
	X-axis, percent	Y-axis, percent	X-axis, percent	Y-axis, percent	X-axis, percent	Y-axis, percent	X-axis, percent	Y-axis, percent
1	57	54	91	88	97	95	99	99
2	39	43	81	81	90	89	95	94
3	58	53	91	84	95	92	97	96
4	68	56	92	92	97	96	99	98
5	70	61	92	93	96	97	98	99
6	58	23	92	85	96	93	98	97
7	57	33	95	90	98	96	99	99
8	53	50	94	89	98	96	99	99
9	65	53	92	87	98	95	99	99
10	47	51	92	92	97	97	99	99
Mean	57	48	91	88	96	95	98	98

For OCD, the fine-tracking control loop was characterized [21], and only the derived models are shown in Fig. 11. As is clear from the figure, a 0-dB bandwidth is about 50 Hz for the x-axis and 60 Hz for the y-axis. Therefore, vibrations above 60 Hz will not be compensated and will even be amplified in a certain frequency range up to several hundred hertz.

The uncompensated beacon motion can be computed following [22]

$$\theta_{\mathrm{rms}} = \sqrt{\int S(f)\ |R(f)|^2 df} \tag{4}$$

where $S(f)$ is the angular beacon-motion power spectral density and $R(f)$ is the tracking-control-loop rejection in the frequency domain. Equation (4) was applied to the computed beacon-motion PSDs, and the results are shown in Table 4 in the uncompensated motion columns. The average uncompensated beacon motion is about 5 μrad for both the x- and y-axis, which is approximately half the total rms motion of 10 μrad. Note that the estimates in Table 1 also include the centroid error of about 1 μrad due to CCD electronic noise and algorithm error [4]. Use of the OLYMPUS spacecraft vibration model with Eq. (4) resulted in an uncompensated motion of 3 μrad as compared with 16 μrad of rms motion. This is because beacon motion is relatively larger at higher frequencies, making compensation more difficult. Figure 10 shows this to be true above 10 Hz.

Uncompensated motion could be determined from the centroid pairs logged by the OCD PC during fine tracking. The centroid pairs are updated at 1 Hz so that power spectral densities of these data cannot be directly compared. When fine tracking was performed, closed-loop operation could be maintained for as long as 1000 s. The main cause of loss of track was due to beacon fades. This was consistent with the laboratory-determined OCD CCD dynamic range of 10.5 dB, as compared with the 13- to 14-dB dynamic range of the intensity fluctuations. Comparisons of the relative beacon and transmit spot centroid pairs was made for times when tracking worked without any fades. The sum of the beacon and transmit spot excursions should add up to zero for perfect compensation. The actual distribution of this sum was

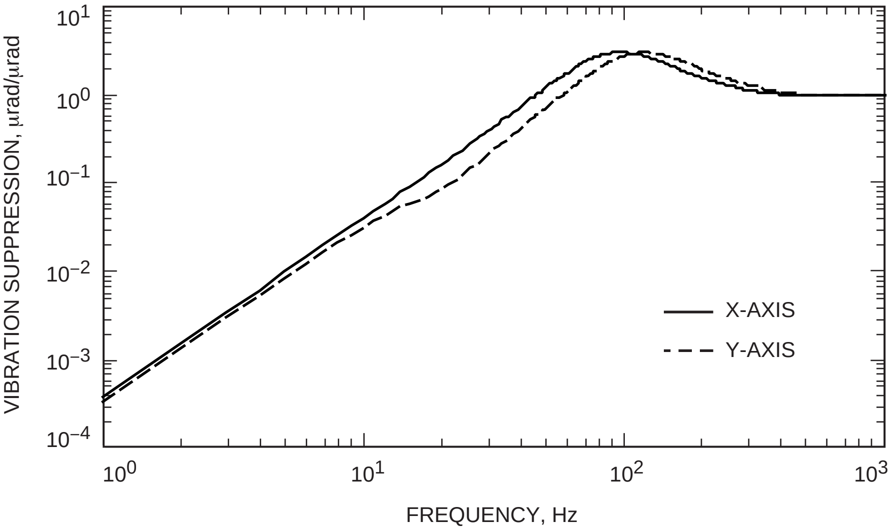

Fig. 11. The derived model for the OCD tracking control loop. The x-axis and y-axis 0-dB bandwidth is 50 and 60 Hz, respectively.

determined, and Table 6 shows the rms value obtained after a Gaussian fit. The extent of agreement observed between the predicted OCD loop performance and that indirectly measured is good.

2. Power Spectral Density of Beacon Intensity Fluctuations. The fluctuations in beacon intensity directly affect the beacon centroid uncertainty [23]. Basically, centroid error is proportional to the inverse square root of beacon intensity, which implies some correlation between beacon intensity fluctuation and motion. The resulting centroid error will appear as beacon motion if not carefully distinguished.

Figure 12 shows two instances of PSDs of x-axis beacon motion along with corresponding intensity fluctuations sensed by the CCD. Although not perfectly correlated, these PSDs do show a 0.67 correlation, which supports the direct relationship between intensity fluctuations and beacon motions. The intensity fluctuations sensed by the CCD sensor shown in Fig. 12 are subject to the dynamic-range limitations mentioned above. The actual temporal fluctuations are better represented by the spectra shown in Fig. 8.

Table 6. Uncompensated error during OCD tracking in June 1998.

Date	Uncompensated x-axis centroid motion, μrad	Uncompensated y-axis centroid motion, μrad
6/17/98	4.81007	6.32446
6/18/98	7.75221	8.52709
6/18(2)/98	9.37	6.18
6/19/98	7.48146	8.3263

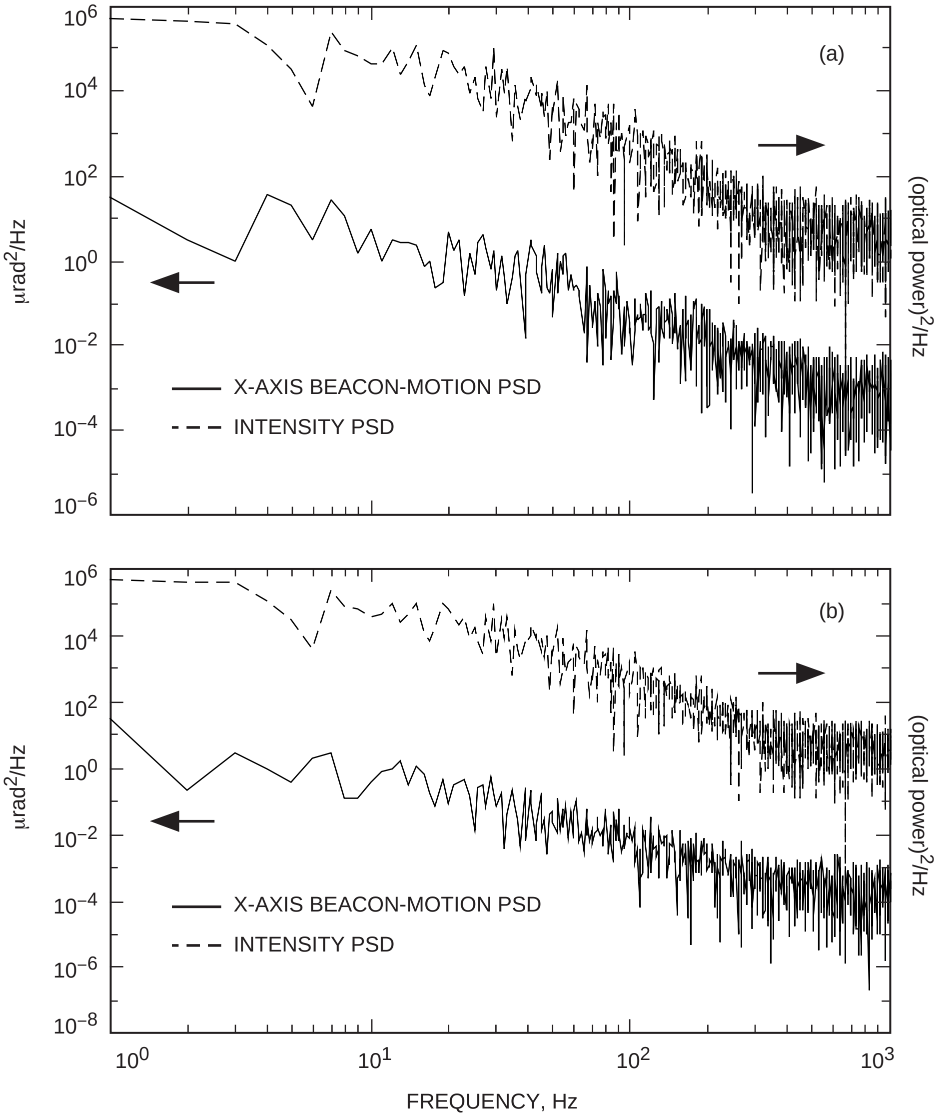

Fig. 12. A comparison of the beacon-motion PSD with that obtained from the intensity-fluctuation data for (a) the largest and (b) the smallest rms beacon x-axis centroid displacement. The partial correlation between the intensity and the beacon motion is consistent with predicted beacon-centroiding performance.

D. End-to-End Link Performance

In Section IV.A, it was shown that, for the multibeam beacon, the σ_I^2 was reduced as compared with a single beam, and that the irradiance fluctuations yielded a lognormal PDF. Likewise, the σ_I^2 for the communications laser when measured below 0.6 yielded a lognormal PDF. In the Appendix, Eq. (A-6) shows the fade probability and mean expected number of fades for a lognormal distribution from which the relation for the mean fade time can be obtained:

$$\text{mean fade time} = \frac{\text{probability of miss}}{\text{mean number of fades}}$$

Table 7 lists these quantities using σ_I^2 and the temporal PSDs measured.

Table 7. The probability of fades below a certain threshold level, with the mean number and duration of the fades.

Beam reception site	σ_I^2	10-dB fade threshold			6-dB fade threshold		
		Probability of miss	Mean no. of fades	Mean fade duration, s	Probability of miss	Mean no. of fades	Mean fade duration, s
TMF	0.07	7×10^{-10}	6.6×10^{4}	1.1×10^{-14}	1.6×10^{-4}	2.5×10^{3}	6.2×10^{-8}
TMF	0.3	2.8×10^{-3}	122	2.3×10^{-5}	0.055	57	9.8×10^{-4}
SP	0.22	4.8×10^{-4}	914	5.3×10^{-7}	0.027	323	8.5×10^{-5}
SP	0.5	0.02	211	9.5×10^{-5}	0.128	133	9.6×10^{-4}

Assuming that the bidirectional fade probability is limited by the beacon on the OCD tracking sensor, Table 7 suggests bit-error rates ranging from 1×10^{-2} to 4.8×10^{-4} for the overall link. As reported in Section IV.A, the received spot size was approximately 200 μm, which was well contained within the 500-μm active area of the APD used. The APD output after clock and data recovery was used to record the BER. The recorded BERs at TMF are shown in Fig. 13 for 40- and 400-Mb/s data streams. The recorded BERs are updated every second and display a fluctuation between two levels bounded by $\sim 1 \times 10^{-2}$ and $\sim 5 \times 10^{-4}$.

The output of the APD detector also was used for viewing eye patterns. The eye-pattern screen of the oscilloscope was recorded on a video tape and played back later for evaluation. Figure 14 displays individual frames extracted from this video record, showing examples of the best- and worst-case eye patterns while transmitting PRBS $N = 7$ at 325 Mb/s. Similar results (not shown) were obtained at data rates up to 500 Mb/s. Qualitatively, the clean eye pattern represented by Fig. 14(a) persisted for several seconds, with intermittent glitches that degraded the eye pattern to that displayed in Fig. 14(b). Usually, when tracking was turned off, the eye pattern degenerated to the appearance shown in Fig. 14(b).

V. Conclusion

Preliminary results obtained while performing a horizontal-path bidirectional optical-link demonstration were reported. Atmospheric scintillation effects were measured at either end of the link. The theoretical bounds provide a basis for what to expect in terms of the scintillation index; however, the bounds span a wide range, as do the measurements, leaving a larger than desirable uncertainty. The lower range of irradiance fluctuation measurements, $\sigma_I^2 < 0.6$, agreed well with a lognormal PDF. Some inconsistencies in theory were also pointed out with the seeing and beam-wander predictions. Performing

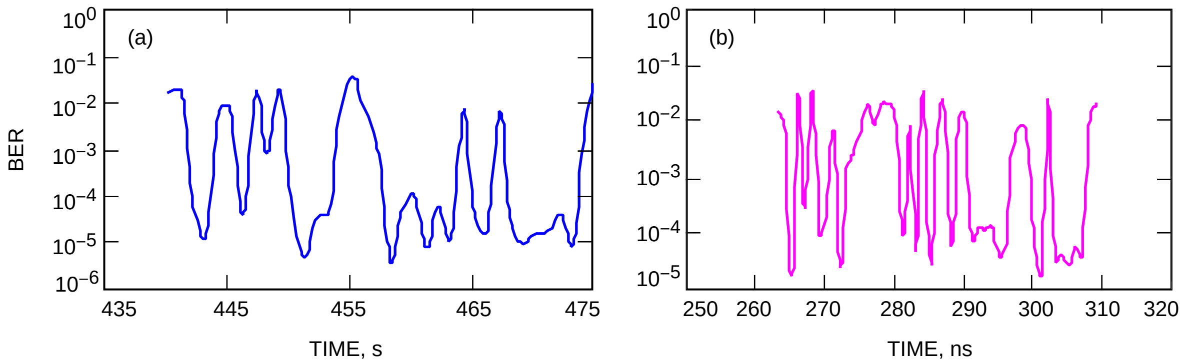

Fig. 13. The BER measurements made at TMF on June 19, 1998: (a) 40 Mb/s, 04:32 A.M. and (b) 400 Mb/s, 04:42 A.M.

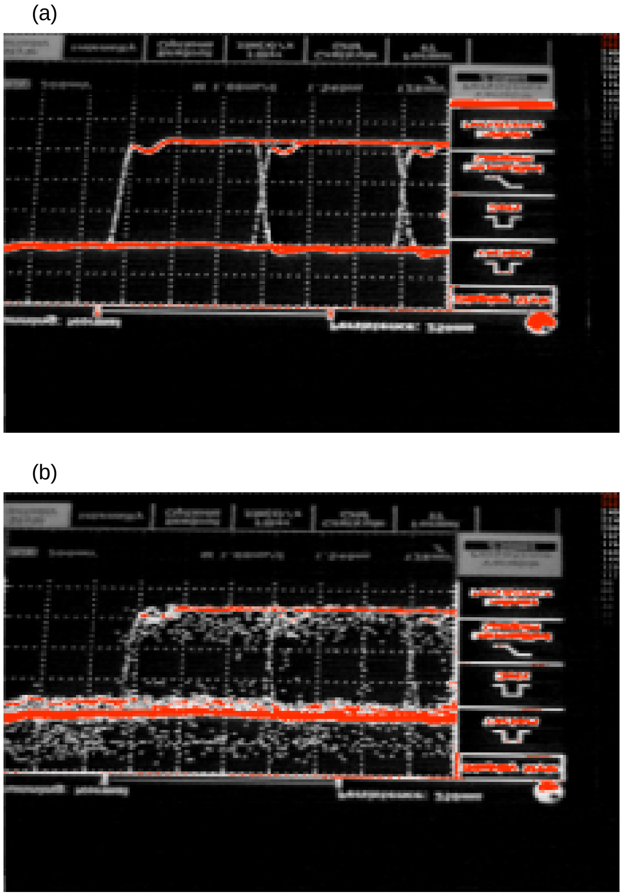

Fig. 14. Typical eye patterns recorded at TMF on June 19, 1998: (a) best case and (b) worst case. Typically, best-case eye patterns persisted for a few seconds, interrupted by the worst-case eye patterns. Without tracking, the worst-case eye patterns were prevalent with occasional appearances of the best case.

more measurements over extended day and night hours while monitoring meteorological conditions can provide a better empirical assessment of atmospheric effects. Even though a lower scintillation index is expected for ground-to-space lower air-mass atmospheric paths, our demonstration showed values as low as 0.07, which are as low or lower than reported for GEO and LEO space-to-ground demonstrations discussed in Section II.A.

Some areas in which the ground-to-ground measurements provide useful systems-level evaluation for optical communications need to be emphasized. The characterization of the OCD fine-tracking loop is one such system. Nominally, the observed uncompensated errors agreed with theory. However, the tracking was sampled only at 1 Hz, while the beacon characterization was not performed simultaneously. This could be improved considerably. Firstly, beacon-irradiance fluctuations must fall within the tracking sensor dynamic range. This could potentially be achieved by using a larger number of beacon beams. As has been shown, the four-beam beacon PDF fits the lognormal distribution, and so fade statistics can be predicted and the tracking loop can be designed to tolerate a reasonable number and duration of fades. Having the ability to log the beacon and transmit laser centroid positions in real time while performing tracking would then provide a self-consistent means of evaluating control-loop performance. The PSD of atmospheric perturbations on beacon centroid motion has been shown to be comparable to the Olympus jitter spectrum, so knowing the performance of the control loop for a horizontal link will provide insight into expected flight performance.

Given the predicted beacon-fade statistics, the observed end-to-end link performance was as expected. However, this also masked possible contributions from beam wander that could have played a role in limiting link performance. By implementing the improvements suggested above to properly characterize fine tracking and then evaluating end-to-end performance, this issue should be clarified.

Acknowledgments

The authors would like to thank M. Jeganathan and H. Hemmati for helpful comments in preparing the manuscript. Thanks to Dr. J. Young of TMF, who helped with operations of the 0.6-m telescope and establishing link alignment. M. Novak, J. Ceniceros, A. Portillo, D. Erickson, J. Depew, B. Sanii, and D. Johnson helped make the reported measurements possible.

References

[1] L. C. Andrews and R. L. Phillips, *Laser Beam Propagation Through Random Media*, Chapters 6 and 7, Bellingham, Washington: SPIE Optical Engineering Press, 1998.

[2] R. R. Beland, "Propagation Through Atmospheric Optical Turbulence," *Atmospheric Propagation of Radiation*, vol. 2 of *The Infrared and Electro-Optical Systems Handbook*, F. G. Smith, ed., Bellingham, Washington: SPIE Optical Engineering Press, pp. 157–229, 1993.

[3] A. Biswas, J. Ceniceros, M. Novak, M. Jeganathan, A. Portillo, D. Erickson, J. Depew, B. Sanii, and J. Lesh, "45 km Horizontal Path Optical Link Experiment," *Free-Space Laser Communications Technologies XI, Proceedings of SPIE*, G. S. Mecherle, ed., vol. 3615, pp. 43–53, 1999.

[4] A. Biswas, M. Wright, A. Portillo, and S. Lee, "Ground–Ground Optical Communications Demonstration," presented at the International Symposium for Deep Space Communications and Navigation, Pasadena, California, September 21, 1999.

[5] M. Jeganathan and S. Monacos, "Performance Analysis and Electronic Packaging of the Optical Communications Demonstrator," *Free-Space Laser Communications Technologies X, Proceedings of SPIE*, G. S. Mecherle, ed., vol. 3266, pp. 33–41, 1998.

[6] M. Jeganathan, A. Portillo, C. S. Racho, S. Lee, D. M. Erickson, J. Depew, S. Monacos, and A. Biswas, "Lessons Learned From the Optical Communications Demonstrator (OCD)," *Free-Space Laser Communications Technologies XI, Proceedings of SPIE*, G. S. Mecherle, ed., vol. 3615, pp. 23–30, 1999.

[7] D. M. Erickson, D. H. Tsiang, and M. Jeganathan, "Upgrade of the Atmospheric Visibility Monitoring System," *Free-Space Laser Communications Technologies XI, Proceedings of SPIE*, G. S. Mecherle, ed., vol. 3615, pp. 310–315, 1999.

[8] L. C. Andrew, R. L. Phillips, C. Y. Hopen, and M. A. Al-Habash, "Theory of Optical Scintillation," *J. Opt. Soc. Am. A*, vol. 16, p. 1417, 1999.

[9] R. L. Phillips and L. C. Andrews, "Universal Statistical Model for Irradiance Fluctuations in a Turbulent Medium," *J. Opt. Soc. Am.*, vol. 72, pp. 864–870, 1982.

[10] J. H. Churnside and R. J. Hill, "Probability Density of Irradiance Scintillations for Strong Path-Integrated Refractive Turbulence," *J. Opt. Soc. Am. A*, vol. 4, pp. 727–733, 1987.

[11] K. E. Wilson, A. Biswas, S. Bloom, and V. Chan, "Effect of Aperture Averaging on a 570 Mbps 42 km Horizontal Path Optical Link," *Atmospheric Propagation and Remote Sensing IV, Proceedings SPIE*, J. C. Dainty, ed., vol. 2471, p. 30, April 1995.

[12] V. Chan and S. Bloom, "Results of 150 km, 1 Gbps Lasercom Validation Experiment Using Aircraft Motion Simulator," *Free-Space Laser Communications Technologies X, Proceedings of SPIE*, G. S. Mecherle, ed., vol. 2699, pp. 60–70, 1998.

[13] R. L. Phillips and L. C. Andrews, "Measured Statistics of Laser-Light Scattering in Atmospheric Turbulence," *J. Opt. Soc. Am.*, vol. 17, pp. 1440–1445, 1981.

[14] C. Higgs, H. Barclay, D. Murphy, and C. A. Primmerman, "Multibeam Illumination," *Lincoln Laboratory Journal*, vol. 11, pp. 8–22, 1998.

[15] J. D. Shelton, "Turbulence-Induced Scintillation on Gaussian-Beam Waves: Theoretical and Observations From a Laser Illuminated Satellite," *J. Opt. Soc. Am. A*, vol. 12, pp. 2172–2181, 1995.

[16] P. A. Lightsey, "Scintillation in Ground-to-Space and Retroreflected Laser Beams," *Opt. Eng.*, vol. 33, p. 2535, 1994.

[17] M. Jeganathan, K. E. Wilson, and J. R. Lesh, "Preliminary Analysis of Fluctuations in the Received Uplink-Beacon-Power Data Obtained From the GOLD Experiments," *The Telecommunications and Data Acquisition Progress Report 42-124, October–December 1995*, Jet Propulsion Laboratory, Pasadena, California, pp. 20–32, February 15, 1996.
http://tmo.jpl.nasa.gov/tmo/progress_report/42-124/124J.pdf

[18] M. Jeganathan, M. Toyoshima, K. Wilson, J. James, G. Xu, and J. Lesh, "Data Analysis Results From the GOLD Experiments," *Free-Space Laser Communications Technologies IX, Proceedings of SPIE*, G. S. Mecherle, ed., vol. 2990, pp. 70–81, 1997.

[19] M. Jeganathan, "Development of the Free-Space Optical Communications Analysis Software," *Free-Space Laser Communications Technologies X, Proceedings of SPIE*, G. S. Mecherle, ed., vol. 3266, pp. 90–98, 1998.

[20] M. Wittig, L. van Holtz, D. E. L. Tunbridge, and H. C. Vermeulen, "In-Orbit Measurements of Microaccelerations of ESA's Communication Satellite OLYMPUS," *SPIE Proceedings, Free-Space Laser Communication Technologies II*, vol. 1218, pp. 205–214, 1990.

[21] C. Racho and A. Portillo, "Characterization and Design of Digital Pointing Subsystem for Optical Communication Demonstrator," *SPIE Proceedings, Free-Space Laser Communication Technologies XI*, vol. 3615, no. 15, pp. 250–261, San Jose, California, January 1999.

[22] E. A. Swanson and J. K. Roberge, "Design Considerations and Experimental Results for Direct-Detection Spatial Tracking Systems," *Optical Engineering*, vol. 28, pp. 659–666, 1989.

[23] S. G. Lambert and W. L. Casey, *Laser Communications in Space*, Boston, Massachusetts: Artech House, Inc., 1995.

Appendix

Summary of Atmospheric Effects on Beam Propagation

The theory presented here is taken from [1] and [2].

For the scintillation index σ_R^2, this Rytov or weak fluctuation theory gives

$$\sigma_R^2 = 1.23 C_n^2 k^{7/6} L^{11/6} \tag{A-1}$$

for a plane wave of wavelength λ and wavenumber $k = 2\pi/\lambda$, range L, and atmospheric structure parameter C_n^2. For a plane wave, $\sigma_I^2 = \sigma_R^2$; for a spherical wave, $\sigma_I^2 = 0.4\sigma_R^2$.

For a Gaussian wave front, the following relation approximates the scintillation index:

$$\sigma_I^2(r, L) \cong 4.42\sigma_R^2 \Lambda^{5/6} \frac{r^2}{W^2} + 3.86\sigma_R^2 \left\{ \begin{array}{c} 0.4\left[(1+2\Theta)^2 + 4\Lambda^2\right]^{5/12} \\ x\cos\left[\frac{5}{6}\tan^{-1}\left(\frac{1+2\Theta}{2\Lambda}\right)\right] - \frac{11}{16}\Lambda^{5/6} \end{array} \right\} \tag{A-2}$$

where the scintillation index is given as a function of r, the radial coordinate of a Gaussian profile; W represents the $1/e^2$ Gaussian beam width at the receiver; and Λ and Θ are Gaussian beam parameters described as $\Lambda = (2L/kW^2)$ and $\Theta = 1 + L/F$, where F is the phase front radius of curvature. The above relation suggests that the additive contribution from the first term for nonzero r (off-axis pointing) will increase the scintillation index given by Eq. (A-1).

These derivations are valid for weak fluctuations restricted to $\sigma_R^2 < 1$. Weak turbulence represents single scattering events with passage of the light wave through the atmosphere. However, with an increase in the path length or strength of atmospheric turbulence, multiple scattering events must be accounted for, giving rise to strong turbulence characterized by $\sigma_R^2 \gg 1$. However, with continued multiple scattering, the beam becomes increasingly less coherent, eventually appearing like extended multiple sources with the onset of saturation, characterized by $\sigma_R^2 \to \infty$. Recently, a heuristic model [7] has been proposed for $0 \leq \sigma_R^2 < \infty$. Before presenting the expressions derived from this theory, certain parameters are introduced, namely the atmospheric spatial coherence length, ρ_0; the Fresnel zone size, $(L/k)^{1/2}$; and a scattering disk or first Fresnel zone, $L/k\rho 0$. In the proposed theory, optical scintillation is modeled as a modulation process in which the small-scale (diffractive) fluctuations are multiplicatively modulated by large-scale (refractive) fluctuations. Moreover, these processes are random and independent. Thus, small-scale contributions are associated with atmospheric cell sizes smaller than the Fresnel zone or the coherence radius, whichever is smaller, and large scale fluctuations are caused by cell sizes larger than the scattering disk. The following expressions were derived:

$$\sigma_I^2 = \exp\left[\frac{0.54\sigma_R^2}{\left(1 + 1.22(\sigma_R^2)^{6/5}\right)^{7/6}} + \frac{0.509\sigma_R^2}{\left(1 + 0.69(\sigma_R^2)^{6/5}\right)^{5/6}}\right] - 1 \tag{A-3a}$$

for a plane wave and

$$\sigma_I^2 = \exp\left[\frac{0.17\sigma_R^2}{\left(1 + 0.167(\sigma_R^2)^{6/5}\right)^{7/6}} + \frac{0.225\sigma_R^2}{\left(1 + 0.259(\sigma_R^2)^{6/5}\right)^{5/6}}\right] - 1 \tag{A-3b}$$

for a spherical wave while neglecting inner scale effects.

With nonzero inner scale effects,

$$\sigma_I^2 = \exp\left[\sigma_{x,p}^2(l0) + \frac{0.509\sigma_R^2}{\left(1+0.69(\sigma_R^2)^{6/5}\right)^{5/6}}\right] - 1 \qquad \text{(A-4a)}$$

for a plane wave and

$$\sigma_I^2 = \exp\left[\sigma_{\ln x,s}^2(l0) + \frac{0.225\sigma_R^2}{\left(1+0.259(\sigma_R^2)^{6/5}\right)^{5/6}}\right] - 1 \qquad \text{(A-4b)}$$

for a spherical wave, where

$$\sigma_{\ln x,p}^2(l0) = 0.15\sigma_R^2\left(\frac{\eta_{x,p}Q_l}{\eta_{x,p}+Q_l}\right)^{7/6} x \left[1 + 7.53\left(\frac{\eta_{x,p}}{\eta_{x,p}+Q_l}\right)^{1/2} - 0.252\left(\frac{\eta_{x,p}}{\eta_{x,p}+Q_l}\right)^{7/12}\right]$$

and

$$\sigma_{\ln x,s}^2(l0) = 0.015\sigma_R^2\left(\frac{\eta_{x,s}Q_l}{\eta_{x,s}+Q_l}\right)^{7/6} x \left[1 + 1.753\left(\frac{\eta_{x,s}}{\eta_{x,s}+Q_l}\right)^{1/2} - 0.252\left(\frac{\eta_{x,s}}{\eta_{x,s}+Q_l}\right)^{7/12}\right]$$

with $Q_l = 10.89L/kl0^2$, $\eta_{x,p} = 3/(1+0.50\sigma_R^2 Q_l^{1/6})$, and $\eta_{x,s} = 8/(1+0.069\sigma_R^2 Q_l^{1/6})$.

A recognized technique to mitigate the effect of atmospheric-turbulence-induced fluctuations on the beacon is to use multiple beams. The beams are mutually incoherent and traverse independent atmospheric paths before overlapping near the receiver aperture. The irradiance fluctuation sensed by the receiver is an incoherent average of the independent beam fluctuations. N beams with measured mean and standard deviation represented by μ_i and σ_i will result in a combined normalized variance of

$$\sigma_{N_{avg}}^2 = \frac{\sum_i^N \sigma_i^2}{\left\langle \sum_i^N \sigma_i \right\rangle^2} \qquad \text{(A-5)}$$

Based on knowledge of the probability distribution function (PDF) of the irradiance fluctuations and knowledge of the scintillation index, σ_I^2, the fade probability for an optical communications link can be determined. The probably of a miss below a specified dB-fade threshold level is described by Eq. (A-6). This is derived based on the lognormal PDF assumption. Mean fade durations and the frequency of fades also can be determined:

$$P_{\text{miss}}(\sigma_I^2) = \frac{1}{2}\left[1 + \text{erf}\left[\frac{\frac{\sigma_I^2}{2} - 0.23 \times \text{fade}_{\text{threshold}}}{\sqrt{2}\sigma_I}\right]\right] \qquad \text{(A-6a)}$$

$$\mathrm{mean}_{\mathrm{fades}} = \nu 0 \exp\left[-\left[\frac{1}{2}\left(\frac{\sigma_I^2 - 0.23\ \mathrm{fade}_{\mathrm{threshold}}}{2\sigma_I^2}\right)\right]\right] \tag{A-6b}$$

where

$$\nu 0 = \frac{1}{2\pi}\left[\frac{\int_0^\infty \omega^2 S(\omega) d\omega}{\int_0^\infty S(\omega) d\omega}\right]^{1/2}$$

with ω being the angular frequency of the temporal irradiance fluctuations and $S(\omega)$ being the PSD of the temporal irradiance fluctuations.

The power spectral density of the intensity fluctuations also is of interest because it can be easily measured. Theoretically, it has been derived as the Fourier transform of the temporal covariance function. Complicated mathematical expressions have been presented to describe the power spectral density of temporal fluctuations; however, these are not shown here. The temporal power spectral density is significant because, under the Taylor frozen atmosphere hypothesis, the temporal statistics can be converted to spatial statistics with knowledge of local wind speed.

The speckle or spatial variations in beam-energy distribution during atmospheric propagation are characterized by spatial coherence length. Asymptotic relations hold for both weak and strong fluctuations in the regimes $\rho 0 \ll l0$ and $l0 \ll \rho 0 \ll L0$. For a Gaussian wave front, these are

$$\rho 0 = \left(\frac{3}{1+\Theta+\Theta^2+\Lambda^2}\right)^{1/2}\left(1.64 C_n^2 k^2 L l0^{-1/3}\right)^{-1/2}, \quad \rho 0 \ll l0 \tag{A-7a}$$

and

$$\rho 0 = \left(\frac{8}{3\left(a+0.618\Lambda^{11/6}\right)}\right)^{3/5}\left(1.46 C_n^2 k^2 L\right)^{-3/5}, \quad l0 \ll \rho 0 \ll L0 \tag{A-7b}$$

where

$$a = \frac{1-\Theta^{8/3}}{1-\Theta}$$

for $\Theta \geq 0$ and

$$a = \frac{1-|\Theta|^{8/3}}{1-\Theta}$$

for $\Theta < 0$.

For plane waves,

$$\rho_{pl} = \left(1.64 C_n^2 k^2 L l0^{-1/3}\right)^{-1/2}, \quad \rho 0 \ll l0 \tag{A-7c}$$

and

$$\rho_{pl} = \left(1.46 C_n^2 k^2 L\right)^{-3/5}, \quad l0 \ll \rho 0 \ll L0 \tag{A-7d}$$

The variance of the angle of arrival or phase-tilt fluctuations for a Gaussian beam can be inferred according to the approximation

$$\sigma_\beta^2 \cong 1.093 C_n^2 L D^{-1/3} \left[a + 0.618 \Lambda^{11/6} \left(\frac{kD^2}{L} \right)^{1/3} \right] \tag{A-8}$$

assuming that $\sqrt{(L/k)} \ll D$.

If all parameters were held constant while varying only the aperture size used to monitor irradiance, then σ_I^2 would get smaller due to aperture averaging, i.e,. spatial averaging of the irradiance fluctuations over many speckles. Several relations have been suggested for the aperture-averaging factor $A = \sigma_I^2(D)/\sigma_I^2(0)$; some of these are shown below:

$$A = \left[1 + \left(\frac{\sigma_I^2}{\sigma_R^2} \right)^{5/7} \left(\frac{kD^2}{4L} \right)^{5/6} \right]^{-7/5} \tag{A-9a}$$

$$A = \left[1 + 1.062 \left(\frac{kD^2}{4L} \right) \right]^{-7/6} \tag{A-9b}$$

$$A = \left[1 + 0.214 \left(\frac{kD^2}{4L} \right)^{7/6} \right]^{-1} \tag{A-9c}$$

where D represents the circular aperture diameter.

The single-axis variance of the beam wander is given by

$$\sigma_c^2 = 1.44 C_n^2 L^3 W_0^{-1/3} \tag{A-10}$$

where W_0 is the initial beam radius. For an isotropic atmosphere, the variance is twice that given by Eq. (A-10).

The effective received beam size, W_e, is given by

$$W_e = W \left(1 + 1.33 \sigma_R^2 \Lambda^{5/6} \right)^{1/2} \tag{A-11}$$

where W would be the size had beam spreading been absent.